12-2019

Synthesis and Characterization of Ion-Implanted Gold Nanoparticles

Nurlathifah Fnu
Western Michigan University, nurlathifahsr@gmail.com

SYNTHESIS AND CHARACTERIZATION OF ION-IMPLANTED GOLD NANOPARTICLES

by

Nurlathifah

A Thesis submitted to the Graduate College
in partial fulfillment of the requirements
for the degree of Master of Arts
Physics
Western Michigan University
December 2019

Thesis Committee:

Asghar N. Kayani, Ph.D., Chair
Paul Pancella, Ph.D.
Ramakrishna Guda, Ph.D.

ACKNOWLEDGEMENTS

First and foremost, I would like to thank you for the presence of Allah SWT who has poured so many favors, gifts, faith, healthiness, and patience. So, I can finish this Master Thesis in a timely manner.

I would like to especially thank to my research supervisor, Dr. Asghar N. Kayani, who has accepted and involved me in his research, mentoring patiently, taught me many new things about material science until this thesis can be completed. I also thank the thesis committee member, Dr. Paul Pancella and Dr. Ramakrishna Guda, who has been willing to discuss in order to improve my thesis. I am also thankful to my instructors and my colleagues for helping me in the lab and became a discussion partner during lectures. I am also grateful to my graduate advisor, Dr. Kirk. T. Korista, who has guided me to be able to complete my program. Robin S. DeHaan, Lori Krum, Josh Byers and Allan Kern, who helped me while I was studying and doing research at the Department of Physics, Western Michigan University.

I would like to give a special thanks to my parents (Sardji and Chotimah), my parents in law (Suharno, alm and Tukiyem, alm), my husband Sugeng Raharjo, who always supports his wife to continue her education and patiently take care of our two children for two years, my beloved sons (Riza and Rama), who have always been my encouragement, also to my entire family especially for my sister, Mbak Laili Nurjannah for the tremendous support and prayer.

I would also like to express my gratitude to the RisetPro Scholarship Program from the Ministry of Research, Technology and Higher Education of Indonesia and my office, the National Standardization Agency (BSN), which has given me a great opportunity to continue my studies. I also would like to thank you to my RisetPro awardee friends, especially to Mbak Anis, Mbak Reny, Reza, Galih, Chulafak and Jali, which always comforts me when I'm down and miss my family, and always encourage me to complete my study.

Nurlathifah

SYNTHESIS AND CHARACTERIZATION OF ION-IMPLANTED GOLD NANOPARTICLES

Nurlathifah, M.A

Western Michigan University, 2019

Gold negative ions of 70 keV energy were implanted within the quartz substrates at room temperature at seven different fluences starting from 2 x 10^{16} particles/cm^2 to 8 x 10^{16} particles/cm^2 with the increment of 1 x 10^{16}. Prior to the implantation, Stopping and Range of Ions in Matter (SRIM) calculations were carried to obtain the Bragg peak below the surface of quartz. Rutherford Backscattering Spectrometry (RBS) was carried out using 2.0 MeV He^{++} ions to measure depth and implanted fluence of gold, and learn how they varied with fluence. Backscattered He particles were recorded by a surface barrier silicon detector at 150^o scattering angle. Exit angle for the RBS measurements was 30^o. UV/Vis measurements were carried out to detect and obtain the Localized Surface Plasmon Resonance (LSPR) of Au nanoparticles with in the quartz substrate.

From RBS data, the Au concentration below the surface of the substrate was observed to increase with the fluence. Increase in fluence creates a higher density of Au atoms in the implant layer, thereby increasing the number of Au nanoparticles developed in quartz. However, saturation in the implanted Au fluence was found to occur at 5 x 10^{16} particles/cm^2. Moreover, as the implanted fluence was increased, Au nanoparticles nucleated closer to the surface of the substrate.

UV/Vis data on the implanted substrates gave the characteristic LSPR peak indicating the formation of Au nanoparticles. Moreover, UV/Vis measurement showed an increase in the optical absorption of the Au nanoparticles with the increase in Au implanted fluence, indicating an increased formation of the Au nanoparticles within the substrate. Also, with the increase in fluence the LSPR peak was redshifted, which could be attributed to either the increase in size of nanoparticles or the formation of hotspots or both.

TABLE OF CONTENTS

LIST OF FIGURES

1. INTRODUCTION

1.1 Nanomaterials

The development of nanotechnology has become a very popular topic over the past decade. It is important because it utilizes very small objects or artifacts, known as nanomaterials [1]. The term “nano” comes from the Greek language and means dwarf. The term nanometer refers to one billionth of a meter (1 nm = 10^{-9} m) [2]. This idea was first described by Richard Feynman in 1959 at the American Physical Society meeting. His lecture titled "There are plenty of rooms at the bottom" accurately predicted the modern direction of nanotechnology and nanoscience [3].

According to the International Organization for Standardization (ISO), nanomaterials are defined as materials with external dimension in the nanoscale (length range approximately from 1 nm to 100 nm) or having an internal structure or surface structure in the nanoscale [4]. Nanoparticles usually refer to approximately spherical particles with diameters within the range of 1–100 nm [5]. An important characteristic that distinguishes nanoscale from bulk is related to scale reduction, which results in materials that have unique properties arising from their nanoscale dimensions [6], namely physical and chemical properties [7]. The most obvious effect associated with scale reduction is a larger specific surface area which implies the presence of relatively more surface atoms. In general, surface atoms are less stable than bulk atoms, which means that the surface of the nanomaterial is more reactive than the bulk [6].

Properties of nanomaterials are very different from those in the bulk, and it all depends on the size and morphology of the nanomaterials [2]. Physical properties of nanomaterials include size, shape, color, size distribution, aspect ratio, morphology, solubility, mechanical strength, optical properties and electrical properties [8].

For electrical properties, when a substance is reduced in size, it changes both the band gap and the distance between adjacent energy levels within the material's electron energy bands. These changes, along with a particle's nanoscale size with respect to the material's mean free path (average distance an electron travels between scattering events), directly affect the electrical resistance of a nanoparticle. More generally, a material's bandgap directly influences whether a particle is a conductor, an insulator, or a semiconductor. For example, take a Carbon Nanotube (CNT), which are produced from a carbon atom formed into tubes with a diameter of only a few nanometers, the smaller diameter CNTs are insulators but at larger diameters, they exhibit metallic properties and act as a conductor [9].

Optical properties, almost the same as electrical properties, are governed by size confinement. The smaller the particles tend to absorb shorter wavelengths, and their absorption spectra shift from red to blue [2]. Metal nanomaterials are sensitive to visible light and ultraviolet (UV), because the shape and size of particles determine the scattering and absorption of light resulting in the color of nanoscale materials. Therefore, nanomaterials are chosen for optical devices such as sensors and displays [8].

1.2 Noble Metal Nanoparticles

On the periodic table, noble metals lie in group 11 of the transition element. Most metal nanoparticles are suspended colloids in a continuous dispersion phase. When light passes through a colloidal solution, particles becomes visible in colors due to certain wavelengths are scattered and some are absorbed. Also, the scattering and absorption of light depends on the nanoparticles surrounding medium because of the difference between the refractive indices [10].

In 1857, Faraday defined the "finely dispersed metal "as a solution for colloidal metals (nano or micro sized particles of metal suspended in liquid) and proposed that the beautiful colors of colloidal gold ascribed to the metallic gold in the form of colloids [5]. British physicist, Thomas Graham in 1861 discovered the term "Colloid" from the Greek word “kolla”, which means glue. Graham classifies the behavior of various chemicals with respect for diffusion they use membranes. In general, colloidal systems are arranged from continuous media and dispersed phases with dissolved particle sizes ranging from 10 nm to 1 μm. In colloids, one substance is spread evenly in another substance. The dispersed substance is called in the dispersed phase, while

the dispersed substance is in the continuous phase [11]. The application of nanomaterials has existed since ancient times, one way being through artistic applications, as shown in the Lycurgus cup (Figure 1) and stained-glass windows for castles and cathedrals [2].

Figure 1. The Lycurgus cup shows different colors depending on the light passing from inside or outside [2]

In the Lycurgus cup, the interaction of light with the surface of the cup containing gold nanoparticles behaves differently, depending on whether illuminated from the inside or outside. When white light interacts with the cup from the outside, bluish green light is scattered by particles and the cup looks dominantly green. Conversely, if light is made from inside the cup, the particles absorb green and the illuminated white light looks translucent red [2] [12].

Noble metal nanoparticles, especially of gold (Au), silver (Ag) and copper (Cu) have attracted great interest from the scientific community because of their spectacular properties and diversity of applications. Noble metals have advantages over other nanoparticles because their optical constants (or dielectrics) are similar to bulk metals until very small dimensions (i.e., < 5 nm) [13]. Also, Au and Ag are resistant to oxidation in moist air and in [14]. Especially, Au is inert, therefore, is biocompatible and is being researched extensively for medical applications. Moreover, they show characteristic colors and unusual optical properties, which are very dependent on the size, shape and dielectric constant of the surrounding medium [14].

1.3 Localized Surfaced Plasmon Resonances

The term plasmon comes from the word plasma, which means gas charged particles. Whereas in the form of metal, plasmons are quantum oscillations of free electron collectors. As

with light consisting of photons, free electron oscillations in metals consist of plasmons. The existence of surface plasmon was first predicted in 1957 by Rufus Ritchie [15]. Surface plasmons are collective charge oscillations that occur at the interface between conductors and dielectrics. They can take various forms, ranging from freely propagating electron density waves (electromagnetic wave) along metal surfaces called Surface Plasmons to localized electron oscillations on metal nanoparticles called Localized Surface Plasmons [16].

Waves sometimes bounce off the surface. Simply put, the wave just hits the surface, for example a wall, then the wave will turn around, and come back. But if you look closely, the wall is still affected. Because several waves seeped into the wall. Disturbances of wave characteristics quickly decay instead of jumping to zero instantly, this is called the evanescent wave [17]. This also applies to metal, free electrons will oscillate when external electromagnetic waves interact with the metal surface. This causes free electrons to vibrate coherently on the metal surface, giving rise to surface plasmons setting an evanescent wave on the surface [18].

The color change in the Lycurgus cup (Figure 1) occurs because of the interaction of metal nanoparticles with electromagnetic (EM) wave and are associated with the unique phenomenon of Localized Surface Plasmon Resonance (LSPR) [12] [19]. LSPR is a characteristic phenomenon of metal nanoparticles, which are produced by electron cloud oscillations on the nanoparticles surface in the presence of the oscillating electric field of EM wave (Figure 2). The instantaneous electric field is generated on the nanoparticles surface as a result of this oscillation that can extend into the dielectric several nanometers in length scale giving rise to an enhanced electric field by several orders of magnitude [14].

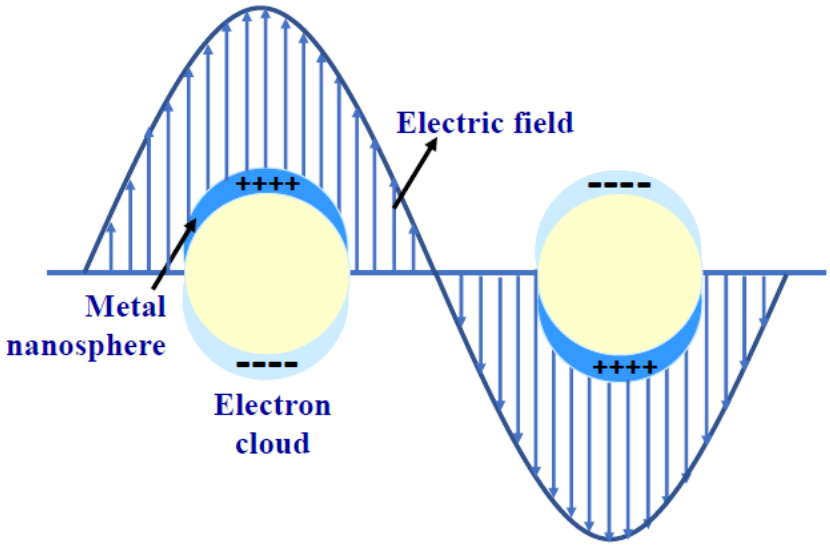

Figure 2. Schematic of Localized Surface Plasmon Resonance [13]

LSPR can give rise to a strong increase in the electric field around the metal surface. This phenomenon leads to the application of LSPR in Surface-Enhanced Raman Scattering (SERS) [20] [21], and increased plasmon-assisted fluorescence [22].

In metal sphere particles with radius a, having homogeneous and isotropic conditions, placed in a uniform electric field $E = E_0\hat{z}$. We assume the surrounding medium has dielectric constants ε_m, is isotropic and does not absorb light. The sphere's dielectric response depends on frequency, given by the dielectric function $\varepsilon(\omega)$, which we take for the moment as a simple complex number ε, as shown in Figure 3 [23].

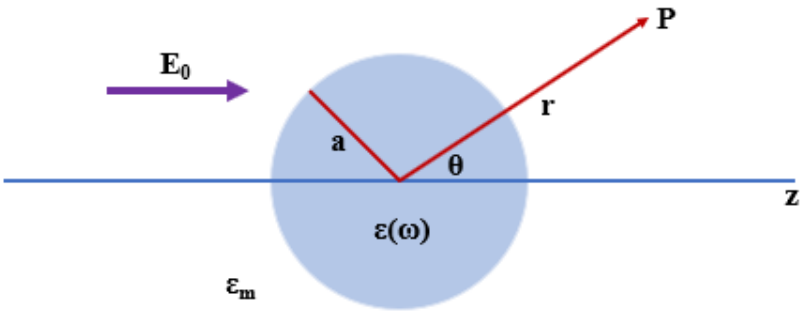

Figure 3. Sketch of a homogeneous sphere placed into an electrostatic field [23]

Through the electrostatic approach, we solve the Laplace equation, $\nabla^2\Phi_1 = 0$, for the potential in the sphere $(r \leq a)$ and outside the sphere $(r > a)$. For inside and outside the sphere, the electric field can be obtained from the scalar potential ($E = -\nabla\Phi$). Because of azimuth symmetry

(not dependent on φ), the general potential solutions for inside and outside the sphere can be written as [24].

$$\Phi(r,\theta) = \sum_{l=0}^{\infty}\left[A_l r^l + B_l r^{-(l+1)}\right] P_l(cos\theta) \qquad (1.1)$$

If the potentials remain finite at the origin, we can rewrite the solution Φ_{in} and Φ_{out} the sphere as [23]

$$\Phi_{in}(r,\theta) = \sum_{l=0}^{\infty} A_l r^l P_l(cos\theta) \qquad (1.2)$$

$$\Phi_{out}(r,\theta) = \sum_{l=0}^{\infty}\left[B_l r^l + C_l r^{-(l+1)}\right] P_l(cos\theta) \qquad (1.3)$$

where the coefficient A_l and B_l can be determined from the boundary conditions at $r = a$ at the surface of sphere and $r \to \infty$ for outside. $P_l(cos\theta)$ is the Legendre polynomials of order l, θ is the angle position vector at point P, in the z-axis. For $r = a$,

$$\Phi_{in} = \Phi_{out} \qquad (1.4)$$

$$-\varepsilon_0 \varepsilon \frac{\partial \Phi_{in}}{\partial r} = -\varepsilon_0 \varepsilon_m \frac{\partial \Phi_{out}}{\partial r} \qquad (1.5)$$

and for $r \to \infty$,

$$\Phi_{out} \to -E_0 r\cos\theta \qquad (1.6)$$

with these boundary condition leads to $A_l = C_l = 0$, for $l \neq 1$, the potentials inside and outside the sphere can be written as

$$\Phi_{in} = -\frac{3\varepsilon_m}{\varepsilon+2\varepsilon_m} E_0 r cos\theta \qquad (1.7)$$

$$\Phi_{out} = -E_0 r cos\theta + \frac{\varepsilon-\varepsilon_m}{\varepsilon+2\varepsilon_m} E_0 a^3 \frac{cos\theta}{r^2} \qquad (1.8)$$

The potential outside the sphere (equation 1.8) describes the superposition of the applied fields ($-E_0 r\cos\theta$) and dipoles located at the center of the particle ($\Phi = \frac{p.r}{4\pi\varepsilon_0\varepsilon_m r^3}$). We can rewrite Φ_{out} as

$$\Phi_{out} = -E_0 r cos\theta + \frac{p.r}{4\pi\varepsilon_0\varepsilon_m r^3} \qquad (1.9)$$

with dipole moment p as

$$p = 4\pi\varepsilon_0\varepsilon_m a^3 \frac{\varepsilon-\varepsilon_m}{\varepsilon+2\varepsilon_m} E_0 \quad (1.10)$$

Therefore, the applied field induces the dipole moment in the scope of magnitude proportional to $|E_0|$. If we introduce polarizability α, then p as

$$p = \varepsilon_0\varepsilon_m \alpha E_0 \quad (1.11)$$

With comparing equations (1.10) and (1.11), the polarization α can be written as

$$\alpha = 4\pi a^3 \frac{\varepsilon-\varepsilon_m}{\varepsilon+2\varepsilon_m} \quad (1.12)$$

The polarization α of a nanoparticle is a valuable parameter because it provides nanoparticle responses to incident light and is directly related with the optical cross section. The extinction cross section is the sum of absorption and scattering cross sections ($\sigma_{ext} = \sigma_{sca} + \sigma_{abs}$). Absorption and scattering cross section can be expressed as functions of the polarization α [25,26]

$$\sigma_{sca} = \frac{k^4}{4\pi}|\alpha|^2 \quad (1.13)$$

$$\sigma_{abs} = kIm\alpha \quad (1.14)$$

where k is wave vector ($k = \frac{2\pi\varepsilon(\omega)}{\lambda}$), volume of a sphere particle $V = \frac{4}{3}\pi a^3$, and dielectric function $\varepsilon(\omega) = \varepsilon_1(\omega) + i\varepsilon_2(\omega)$, the extinction cross section can be written as [27]

$$\sigma_{ext} = 9\frac{\omega}{c}\varepsilon_m^{3/2} V \frac{\varepsilon_2}{(\varepsilon_1+2\varepsilon_m)^2+\varepsilon_2^2} \quad (1.15)$$

where ε_1 and ε_2 are imaginary part and real of the electric function of the sphere.

Polarization increases and reaches a maximum when $|\varepsilon + 2\varepsilon_m|$ is minimized, which occurs between the conduction band electrons and the incident field. This condition is called the Fröhlich condition as

$$(Re[\varepsilon(\omega)] = -2\varepsilon_m) \quad (1.16)$$

where there is an increase in the local plane around the metal nanoparticles [23]. From the theory of scattering and absorption of radiation from small spheres one can predict an increase in the resonance field due to the resonance of beyond the Quasi-Static Approximation and Lifetime Plasma Polarizability α (1.12), if the Fröhlich condition (1.16) is satisfied. In this condition, nanoparticles act as electric dipoles, absorbing and scattering electromagnetic fields in a resonant manner. All of the above equations are for calculating estimates based on static approximations, where the wavelengths of the incoming light are greater than the size of the sphere.

In 1908, Gustav Mie developed a complete theory of scattering and absorption of electromagnetic waves interacting with the metal sphere, which is now known as Mie theory. This theory reveals incident electric and magnetic fields that are spread inside and outside the sphere through a series of expansions in spherical harmonic vectors. A valid quasi-static result for the sub-wavelength sphere is then restored by expanding the power circuit of the absorption and scattering coefficients and only maintaining the first term [23].

The size of the structure of metal nanoparticles is one of the important factors that determine plasmonic resonance, because the size of nanoparticles has a dramatic effect on plasmonic behavior. This can be seen with the increasing diameter of spherical nanoparticles leading to the corresponding red-shift in the plasmonic response, meaning that the resonance will shift to a longer wavelength (Figure 4). When the wavelength increases, the frequency decreases. Resonance shift occurs when the oscillation path of electrons moving together becomes larger. Larger particles will support longer periods of electron oscillation in collective motion due to an increase in the distance of motion [28].

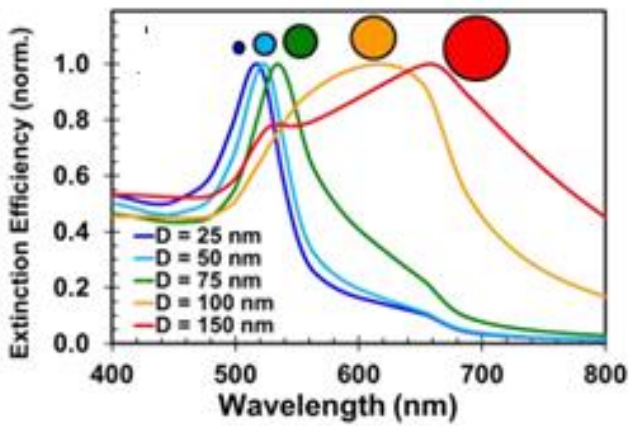

Figure 4. Normalized extinction efficiencies for various sizes of gold nanospheres in water. The circles above the plot correspond to the relative cross-sectional area of the spheres simulated [28]

Small-sized nanoparticles will dominate the absorption cross-section efficiency, while larger-sized nanoparticles will dominate the scattering cross-section efficiency, as shown in Figure 5. Figure 5 shows the absorption cross section of 50 nm gold nanoparticles much higher than the scattering cross-section. While gold nanoparticles with a size of 150 nm dominate the scattering cross section [28].

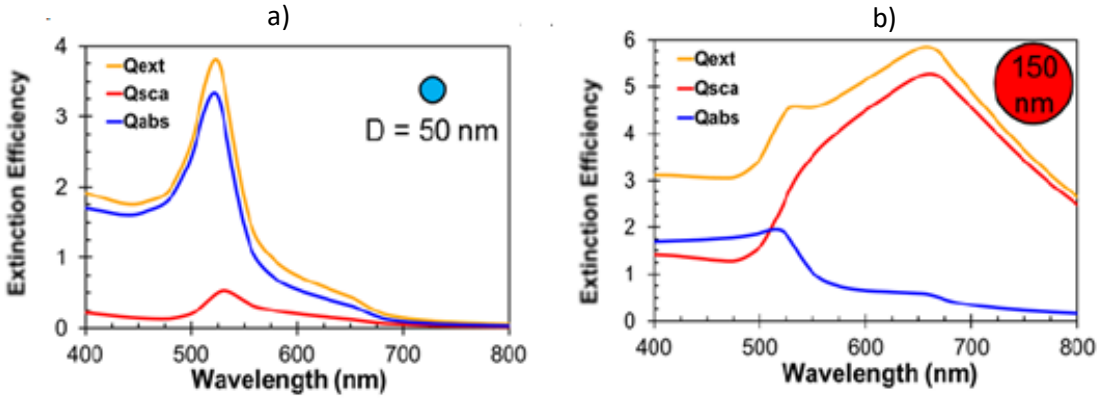

Figure 5. Interaction efficiencies for two different sizes of gold nanospheres in water. a) 50 nm gold nanosphere in water, and b) 150 nm gold nanosphere in water [28]

In this thesis, we synthesize Au metal nanoparticles with low energy (70 keV) ion-implantation process in quartz. Rutherford Backscattering Spectrometry (RBS) to determine the concentration of Au and obtain actual implanted fluence. UV/Vis spectroscopy is used to confirm formation of gold nanoparticles. Effect of increasing ion beam fluence on the distribution and optical absorption of gold nanoparticles is studied and subsequent conclusions are drawn.

2. EXPERIMENTAL METHODS

In this section, we discuss about the experimental methods employed to synthesize and characterize the ion-implanted gold nanoparticles.

2.1 Synthesis of Gold Nanoparticles

There are various ways to synthesize metal nanoparticles in dielectrics, one of which is ion implantation. Ion implantation is a process by which virtually any element can be injected into the near-surface region of any solid by means of a beam of high-velocity ions, usually tens to hundreds of kilo-electron-volts in energy, striking a target mounted in a vacuum chamber. The incident ions stop at a certain depth in the host material as a result of energy loss during collisions with the substrate atoms. The concentration-depth profile produced from implanted dopant atoms can be calculated for most of the target-projectile combinations from theoretical considerations. In low ion fluids (e.g., number of ions per unit area), depth concentration profiles are usually well characterized by a Gaussian distribution centered on the average range [29].

The basic elements needed in the implantation system are an ion source, acceleration column, mass-separator, and target chamber. With different types of ion sources, a wide variety of beams may be produced with sufficient intensity for implantation purposes; 10^{14} ions cm^{-2} to 10^{16} ions cm^{-2} (less than a 'monolayer') is a representative ion dose. Ion dose is defined as the number of ions cm^{-2} implanted into the sample. Alternatively, the term fluence is used instead of dose. The ion beam current density is expressed in units of A cm^{-2} [30]. As the dose of incident ions increases, the concentration of implanted atoms increases, thus modifying the near-surface composition of the target [31].

Embedding metal ions in the dielectric by means of ion implantation and subsequent annealing provides a degree of control over particle size, and depth. An important advantage of ion implantation compared to other synthetic methods is the ability to achieve a high metal filling

factor, beyond the metal solubility of the target matrix [30]. Ion implantation can also induce matrix structural defects in the form of vacancies, interstitials and dislocation loops.

For our experiments, the first step for ion implantation is the ion beam that was produced from the Source of Negative Ions by Cesium Sputtering (SNICS II) connected to a 6.0 MV Tandem Van de Graaff accelerator of the Western Michigan University (WMU) (Figure 7). For the ion implantation in this study we used gold powder (Au) as the source cathode to extract negative ions to be bombarded on a quartz substrate. The cathode is made of copper and Au powder is compacted in the cathode cup. Cathode is place at -6 kV with respect to the local ground and was cooled. Cesium (Cs) from the oven was ionized by the electrons from the ionizer and sputters the Au in the cathode. Cs also forms a layer on the cold cathode that donates electrons and the ejected Au atoms picks up an electron to become Au^-. The schematic of ion source (SNICS II) can be seen in Figure 6.

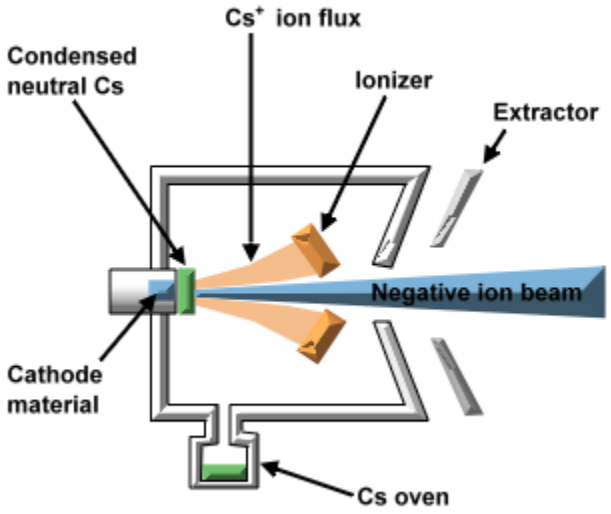

Figure 6. Ion source schematic [32]

The Au ion beam is extracted, focused, accelerated and filtered by a 20^o injection magnet in to Low Energy (LE) beamline. The Einzel lens further focuses the beam through +50 V biased (to suppress secondary electrons) 5 mm x 5 mm collimator on to LE Faraday cup, which is later removed from the path for the beam to be bombarded on the substrate. The substrate is placed on the LABview controlled precision XY stage, which moves the stage using horizontal and vertical stepper motors in front of the beam for Au implantation (Figure 8). The sample holder is biased at

+50 V and area of implantation was selected to be 3.5 cm^2. The experimental set up for the LE ion implantation is shown in Figure 9.

Figure 7. 6.0 MV Tandem Van de Graaff Accelerator at WMU

Figure 8. The XY stepper motors

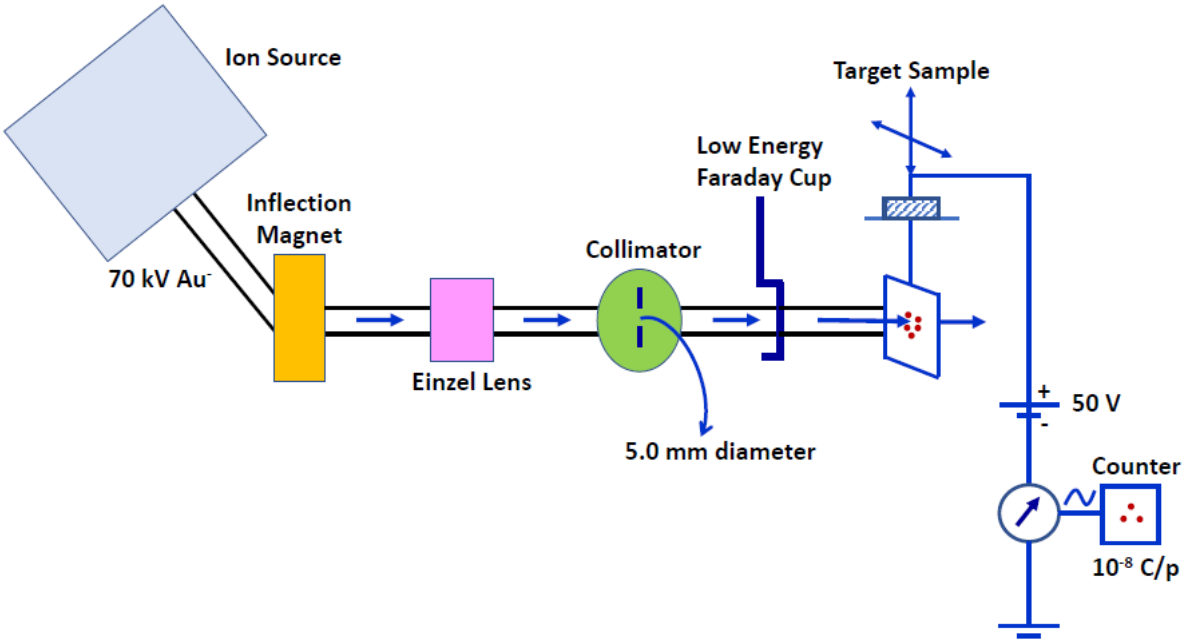

Figure 9. Schematic of the experimental set up for the low energy ion implantation

A digital current integrator is used to measure DC current on the target and the current was integrated to get the desired charge on the sample holder. We used 10^{-8} Coulomb/pulse to calculate the desired fluence on the target. A counter is used to record the total number of pulses coming from the current integrator. The fluence was calculated from the total charge accumulated on

sample divided by the electronic charge and the area in cm^2. The results of the Au ion-implanted substrates are given in the Figure 10.

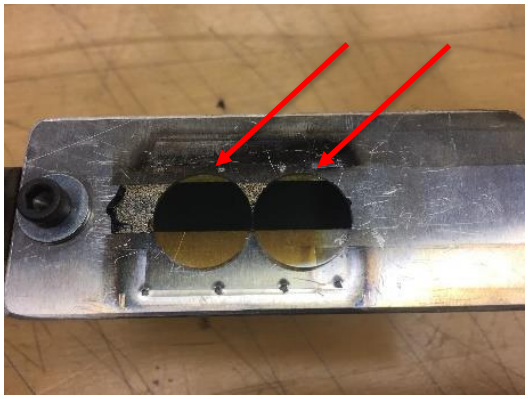

Figure 10. Target sample of ion-implanted Au nanoparticles

For our experiment we selected circular fused quartz (SiO_2) of 1 mm thickness and 10 mm diameter and the energy of the Au^{-1} ions was 70 keV. The ion implantation for the all the substrates was carried out at room temperature. Quartz is used because it is transparent for wavelengths ranging from 190 to 2500 nm [33] therefore, does not absorb light in the wavelength range of Au nanoparticles. Before implantation, quartz samples were cleaned with acetone to remove the surface contaminants and then implantation was taken place for different fluences. Ion energy was selected by the Stopping and Range of Ions in Matter (SRIM) calculations.

2.2 Rutherford Backscattering Spectrometry

Rutherford backscattering spectrometry (RBS) is one of the methods used as a general diagnostic and analytical tool for material analysis, which makes use of the accelerators [34]. It is an important tool to analyze the near surface structure and composition of the target and is based on the backscattering of high-energy ions, usually alpha or protons. This method is quantitative and non-destructive [35]. The RBS technique is often applied to the fields related to material analysis, such as those that investigate thin surface structures, crystal orientation and crystal damage.

When a sample is bombarded with a beam of high energy particles, most of the particles are implanted into the material and do not escape. A small portion of them interact with the nucleus of an atom. This interaction is electrostatic and does not involve direct contact between the

projectile ion and the target atom. It can be modeled accurately as elastic collisions using classical physics theory [36].

The RBS experiment was carried out using 6.0 MV tandem van de Graaff accelerator facility at Western Michigan University (WMU) and the setup is shown in Figure 11. The electronics include a preamplifier, an amplifier, an Analog-to-digital ADC, a multichannel analyzer (MCA). A counter that receives signals from the current digitizer is used trigger the MCA for data acquisition [34]. The experimental RBS data obtained is simulated with SIMNRA to obtain the concentration and depth profile of ion-implanted gold in quartz substrate [37]. RBS was carried out with 2.5 MeV He^{++} ions at room temperature. Helium ions were produced from Radio Frequency (RF) source and accelerated through the accelerator. For guiding and focusing same setup is used as was used for the beam coming from SNICS II. The target chamber is an electrically isolated high vacuum circular chamber having two upstream collimators.

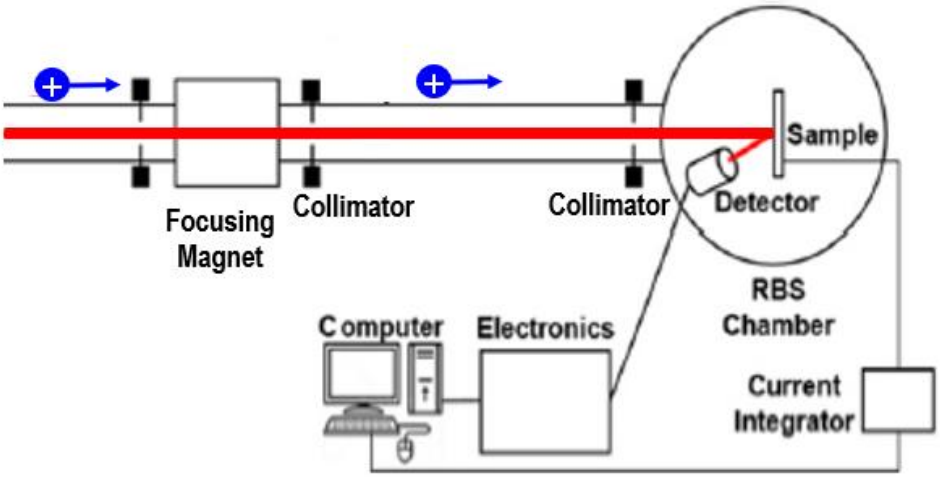

Figure 11. Schematic of the accelerator facility used for RBS analysis [34]

This chamber is provided with a turn table that can be moved from outside that provides the option of changing the scattering angle. The detector was placed on the turntable at 150^{o} scattering angle and 2.5 mm collimators was used for RBS data. The target sample was placed on a sample holder and biased at 180 V battery to suppressed secondary electrons. The beam intensity on the target was set at 10 - 15 nA. Low ion beam currents help to stop the pile-up effect during the process of detecting backscattered particles. Pile-up arises when the detector system time response is not fast enough to distinct the individual events on the detector due to the high rate of encountered events. Consequently, in such situation two events may end up being recorded as one

event, which leads to false measurements. A digital current integrator is used to record the total accumulated deposited charge on the target (for RBS experiment, 10^{-10} Coulomb/pulse is used). Backscattered helium particles were collected at 150^{o} scattering angle and incident and exit angles were set at 0^{o} and 30^{o} respectively. The detector used was a surface barrier silicon detector which were obtained from ORTEC with model number BU-012-050-100. The surface barrier silicon detector of energy resolution of 12 keV operates at a reverse bias with the bias voltage of 40 V. A pre-amplifier is placed close to the detector which gives a reverse current upon the arrival of backscattered He from the target. The current from the preamplifier is converted into the voltage pulse in direct proportion to the backscattered energy. A spectroscopy amplifier which further amplifies the input voltage pulse from the preamplifier.

Signals from the spectroscopy amplifier is digitized by Analog-to-digital ADC and the Multi-Channel Analyzer (MCA) places the digitized input at the corresponding energy of the backscattered event on horizontal axis. The ADC can take voltage signals of 10 V or less, therefore the gain of the spectroscopy amplifier was set to keep the voltage signals less than 10 V. The plot from MCA consists of counts versus channel numbers and a calibration factor was calculated to convert the scale to energy [35].

2.3 UV/Vis Spectroscopy

UV/Vis spectroscopy is a technique that readily allows one to determine the optical absorption properties of a material. Therefore, UV/Vis spectroscopy is widely used for quantitative analysis of all molecules that absorb ultraviolet and visible electromagnetic radiation [38].

The absorption of visible and ultraviolet (UV) radiation is associated with electron excitation, both in atoms and molecules, from lower to higher energy levels. Because the energy level of matter is quantized, only light with the right amount of energy can cause a transition from one level to another to be absorbed. UV/Visible spectrometers can be used to measure the absorbance of ultra violet or visible light by a sample, either at a single wavelength or scan at a range in the spectrum. The UV region ranges from 190 to 400 nm and the visible region is from 400 to 800 nm. This technique can be used both quantitatively and qualitatively [38].

For the characterization of Au nanoparticles, absorption measurements were carried out using Lambda 35, UV/VIS Spectrometer absorption spectrophotometer with 1.0 nm slit width (spectral band width) (Figure 12). The measurements were carried out at room temperature and the absorption spectrum for all ion implanted samples were collected in the wavelength range from 200 nm to 1100 nm.

Figure 12. UV/Vis Spectroscopy at Physics Department, WMU

3. EXPERIMENT AND CHARACTERIZATION

3.1 Rutherford Backscattering Spectrometry

For this RBS experiment, we used samples Au implanted in substrate with different fluences from 2×10^{16} particles/cm^2 to 8×10^{16} particles/cm^2. The RBS data was simulated and analyzed by using the SIMNRA simulation. The composition and areal density are calculated by fitting the experimental data by mean of the simplex algorithm. A representative RBS experimental and simulated plot for fluence equal to 5×10^{16} particles/cm^2 is shown in Figure 13 as an example.

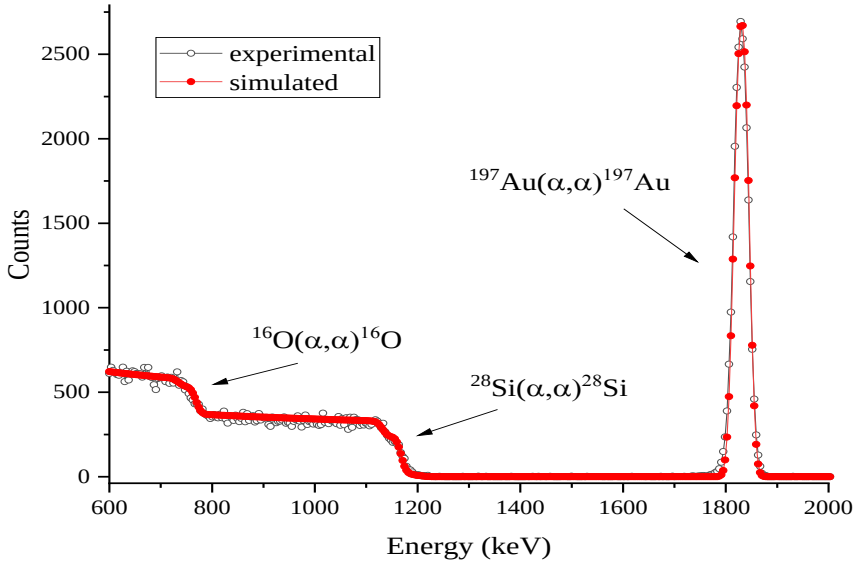

Figure 13. Experimental and simulated RBS spectra for fluence 5 x 10^{16} particles/cm^2

3.2 UV/Vis Spectroscopy

The optical characterization of the implanted substrates was carried out with UV/Vis spectrometer. Spectrometer was turned on for about 20 minutes to warm up and background was scanned with the bare quartz which was recorded. We then put the quartz substrates on a UV/Vis spectrometer and performed the measurement with a wavelength range of 200 - 1100 nm and the saved background was subtracted for the data This is done for all samples and data was plotted in the Origin version 2019 for analysis. The result of the UV/Vis plot for fluence 8 x 10^{16} can be seen

in Figure 14 which gives a characteristic absorption peak that indicates the formation of Au nanoparticles within the substrate.

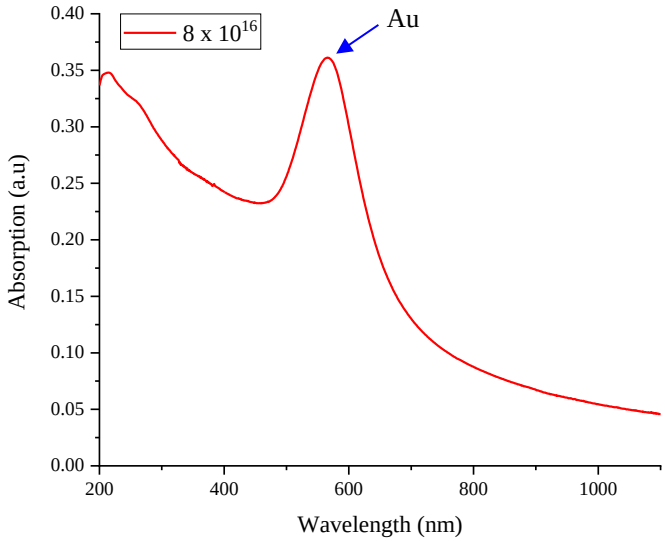

Figure 14. UV/Vis plot for samples 8 x 10^{16} particles/cm^2

.

4. RESULTS AND DISCUSSION

In the previous chapter, the details of the equipment used and the processes carried out to synthesize and characterize Au implanted is explained. In this chapter, the experimental results, analysis and the discussion of UV/Vis and RBS data are given.

4.1 Optical Absorption Measurements

Optical absorption measurements were used to obtain UV/Visible absorption spectra of the 70 keV implanted quartz substrate with different fluences (2 x 10^{16} particles/cm^2 to 8 x 10^{16} particles/cm^2) and are shown in Figure 15. The characteristic surface plasmon absorption bands were observed for all the implanted substrates, which confirms the presence of Au nanoparticles. Moreover, with the increased fluence, absorbance was found to be increasing as well. Highest absorbance was found for a substrate implanted with 8 x 10^{16} particles/cm^2.

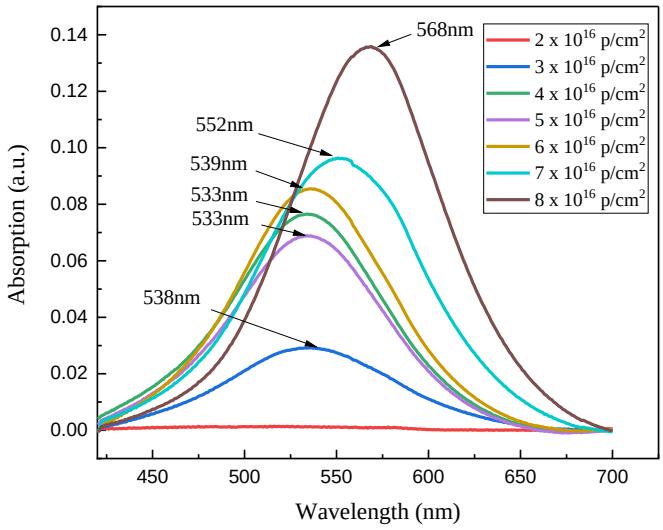

Figure 15. Surface plasmon resonance spectra of ion-implanted gold nanoparticles synthesized at different ion beam fluences

No change in the LSPR peak positions for the substrates implanted with 3 x 10^{16} particles/cm^2 to 6 x 10^{16} particles/cm^2 was observed. However, peak areas increased. This indicates that these substrates probably have same size Au nanoparticles but the number of nanoparticles is increasing. Peak positions for the substrates implanted from 6 x 10^{16} particles/cm^2 to 8 x 10^{16} particles/cm^2 fluence redshifted from 533 nm to 568 nm. With the increase in the size of nanoparticle, the LSPR peak gives rise to redshift that can be explained using Mie theory. Moreover, since the number of nanoparticles is increasing in these substrates, inter-nanoparticle distance can decrease, creating hotspots [39] (as shown Figure 16), which can also contribute to the redshift. We also observed that the width of the LSPR peak increased for the substrates implanted from 6 x 10^{16} particles/cm^2 to 8 x 10^{16} particles/cm^2 fluence, which is consistent with the Mie theory [40], which says that with the increase in the size of nanoparticles, scattering cross section also increases. Non-uniform size distribution of nanoparticles can also cause differences in the wide Au LSPR peak [41].

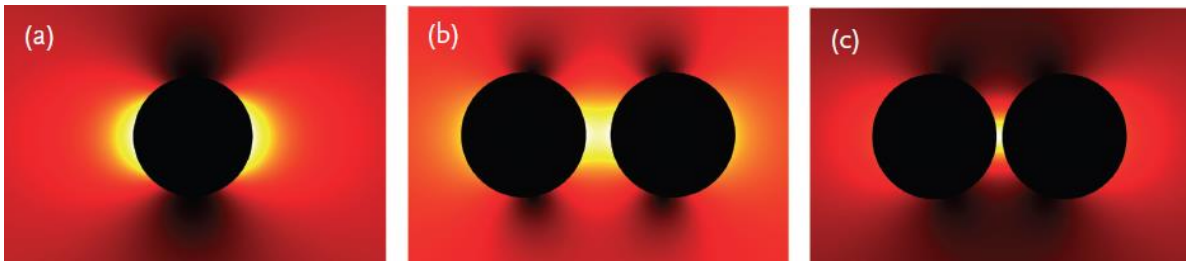

Figure 16. (a) Single Au nanoparticle, (b) two Au nanoparticles with 4 nm gap, and (c) two Au nanoparticles with 1 nm gap [39]

4.2 Rutherford Backscattering Spectrometry

The Au concentration profile of the sample implanted in silicon quartz was obtained from RBS carried out using the WMU 6.0 MV Tandem Van de Graaff accelerator. The RBS measurements of Au implanted quartz substrates were performed using 2.0 MeV He^{++} ions.

RBS measurements were carried out for 7 substrate that was implanted with differences fluences from 2 x 10^{16} particles/cm^2 to 8 x 10^{16} particles/cm^2. From the plots, it can be seen that fluence with 8 x 10^{16} particles/cm^2 has a higher peak compared with fluence of 5 x 10^{16} particles/cm^2 and 2 x 10^{16} particles/cm^2, that show the nucleation of Au nanoparticles is towards the surface of the substrate. The Au concentration within the quartz substrate was estimated by simulating the experimental RBS data with SIMNRA [37]. The analysis is carried out using a

SIMNRA simulation package, where the data channel must first be converted into energy using the following equation [37]:

Energy (keV) = the Calibration Offset (keV) + [the Energy per Channel (keV / channel) x channel]

In the Figure 13, the experimental RBS spectrum (black line) and the simulated spectrum (red line) is given. The horizontal axis is energy scale in keV which gives the energy of backscattered He into the detector. Vertical axis gives the counts. The area under the peak (or curve) gives the number events of incident He ions (1836 keV) backscattered with atoms in near surface region of the substrate. Figure 13 shows a peak that corresponds to the He backscattered from Au within the quartz substrate. The Si and O edge of the substrates are at 1212 keV and 739 keV. For the beam, substrate is an infinite medium. Incident He ions eventually lose energy within the substrate and cannot backscatter; therefore, we get edges for Si and O in the RBS spectra of the Au implanted quartz substrate.

Table 1. Elemental concentration of ion-implanted Au within substrate

Sample	Expected fluence (particles/cm^2)	RBS Areal density (particles/cm^2)	Concentration Si Layer 1 (%)	Concentration O Layer 1 (%)
1	8.00 x 10^{16}	4.42 x 10^{16}	34	66
2	7.00 x 10^{16}	4.84 x 10^{16}	34	66
3	6.00 x 10^{16}	4.72 x 10^{16}	34	66
4	5.00 x 10^{16}	4.84 x 10^{16}	34	66
5	4.00 x 10^{16}	3.73 x 10^{16}	34	66
6	3.00 x 10^{16}	2.75 x 10^{16}	34	66
7	2.00 x 10^{16}	2.07 x 10^{16}	34	66

The Figure 17 in the overlapped Au peaks in RBS experimental spectra for all the implanted samples. It can be seen that Au peak area increases for the substrates that were implanted with increasing fluence, indicating the increased Au concentration. From the simulation of the experimental RBS spectra, it was found that implanted Au was embedded below the surface of the substrate, however, as the Au fluence within the substrate was increased, Au accumulated closer

to the surface. This is evident from the Figure 17 that the leading edge of the Au peak is moving towards right on the horizontal energy scale (1828 keV to 1836 keV). From the UV/Vis measurements, we already know the Au nanoparticles are formed during the implantation process. From RBS, we see that Au is found closer to the surface for high fluence Au implanted substrate which indicates that newly nucleated Au nanoparticles are forced closer to the surface. Moreover, from the simulation of RBS spectra we see that the areal density has a saturation of 5 x 10^{16} particles/cm^2 (as shown in Table 1). When the fluence exceeds ~ 6 x 10^{16} particles/cm^2, the results show that areal density has a maximum value of 5 x 10^{16} particles/cm^2. This means that the metal filling factor has saturated which does not allow areal density to be higher than 5 x 10^{16} particles/cm^2.

Figure 17. Overlapped Au back scattered peak for all the implanted substrates

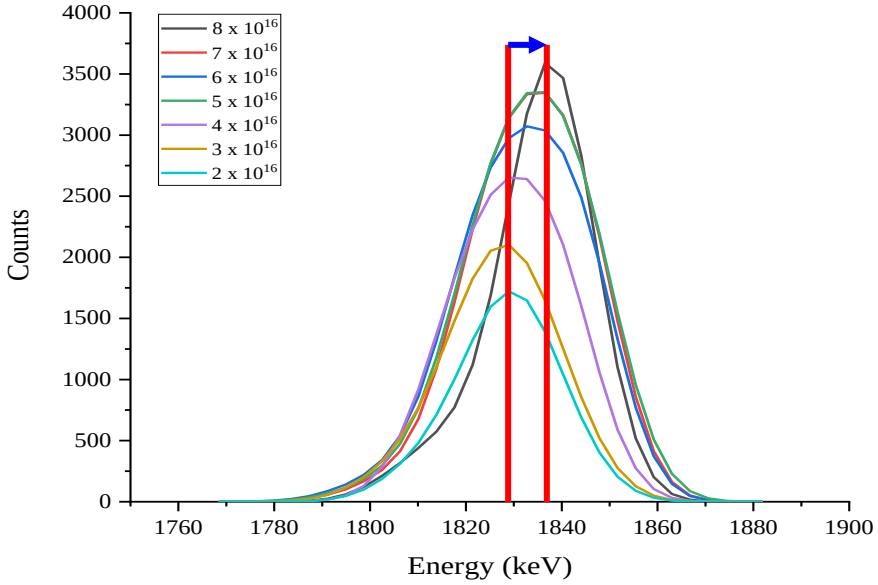

5. CONCLUSIONS

The interest in the study of noble metal nanoparticles, especially gold, is growing rapidly. In this thesis, we synthesized and studied the optical properties of Au nanoparticles implanted in quartz substrate. Synthesis was carried out using 70 keV Au^- ions and the quartz substrates were implanted with different fluences. Negative Au ions were produced by a SNICS II ion source and the ion energy was selected based on SRIM calculations. The study was conducted for 7 samples in quartz substrate with differences fluence from 2 x 10^{16} particles/cm^2 to 8 x 10^{16} particles/cm^2. The Au implanted quartz substrates were characterized by UV/Vis and RBS measurements.

From the UV/Vis measurements was confirmed the formation of Au nanoparticles in ion implanted in quartz substrate and found that an increase in the ion implanted fluence assisted in making bigger size nanoparticles. The redshifted LSPR peak for substrates implanted with higher fluence in indicative of increasing the size of nanoparticles. We also found that for the substrates implanted with fluence greater than 5 x 10^{16} particles/cm^2, formation of hot spots could also contribute to the redshift in the LSPR peak. Since the increasing fluence increases the number of nanoparticles within the substrate, inter-nanoparticle distance can decrease, creating hotspots. The LSPR peak width was also found to be increasing with ion implanted fluence. This could be because of the non-uniform size distribution of nanoparticles or the increased scattering cross section of bigger nanoparticle size. The highest absorption peak of Au implanted was found with fluence 8 x 10^{16} particles/cm^2 with peak position at 568 nm.

The RBS measurement was carried out with 2.5 MeV He^{++} ions. The incident and exit angles of 0^o and 30^o were used and the detector was placed on 150^o scattering angle collect the backscattered helium particles. The experimental data was simulated with the SIMNRA package. From the SIMNRA data, we obtained the areal density of Au implanted in quartz substrate.

We conclude that the nucleation of Au nanoparticles within the substrates takes place during the implantation process, therefore, newly created nanoparticles moves closer to the substrate surface. This is evident from the Figure 17 that shows that with the increase in the ion implanted fluence, the Au peak edge moved from 1828 keV to 1836 keV and the nucleation of Au nanoparticles is towards the surface of the substrate. From SIMNRA simulation, when the fluence exceeds ~ 6 x 10^{16} particles/cm^2, the results show that areal density has a maximum value of 5 x 10^{16} particles/cm^2. This is because the metal filling factor does not allow fluence to be higher than 5 x 10^{16} particles/cm^2 for the particular energy used for Au implantation in fused quartz.

REFERENCES

[1] The Scientific Committee on Emerging and Newly Identified Health Risks (SCENIHR). (2009). "Nanomaterials". Retrieved from https://ec.europa.eu/health/scientific_committees/opinions_layman/nanomaterials/en/index.htm

[2] Vatjai, R. (2013). "Science and Engineering of Nanomaterials". In Vajtai, R. (Eds), *Springer Handbook of Nanomaterials* (pp. 1 - 31)

[3] Martinsson, E. (2014). *Nanoplasmonic Sensing using Metal Nanoparticles*.

[4] ISO/TS 8004.1. (2015). *Nanotechnologies – Vocabulary – Part 1: Core terms*. International Organization for Standardization.

[5] Tan, Y., Li, Y., and Zhu, D. (2004). *Noble Metal Nanoparticles*.

[6] Tantra, R., Jarman, J. C., and K. N. Robinson. 2016. "Introduction". In Tantra, R. (Eds), *Nanomaterial Characterization – An Introduction (Chapter 1)*.

[7] Rao, C.N.R. and Cheetham, A.K. (2006). "Materials Science at the Nanoscale". In Gogotsi, Y. (Eds), *Nanomaterials Handbook (Chapter 1)*.

[8] Reghunadhan, A., Kalarikkal, N., and Thomas, S., 2018. "Chapter 7 - Mechanical Property Analysis of Nanomaterials". Bhagyaraj, S.M, et al (Eds). Characterization of Nanomaterials: Advances and Key Technologies (pp. 192 - 212).

[9] Niemann, J., (2005). *Electrical Measurements on Nanoscale Materials*. Keithley Instruments, Inc.

[10] Singh, A. K., (2016). "Chapter 2 - Structure, Synthesis, and Application of Nanoparticles". ScienceDirect, *Engineered Nanoparticles: Structure, Properties and Mechanisms of Toxicity (pp 19 - 76)*.

[11] López-Esparza, R. Altamirano, M. A. Balderas, Pérez, E. and Goicochea, A. Gama. (2015). "Importance of Molecular Interactions in Colloidal Dispersions". *Advances in Condensed Matter Physics*, Volume 2015.

[12] Martinsson, E., (2014). *Nanoplasmonic Sensing using Metal Nanoparticles*.

[13] Feldheim., D. L. and Foss Jr., C.A. (2002). “Overview”. In Feldheim and Foss (Eds). *Metal Nanoparticles: Synthesis, Characterization and Applications (pp. 1 - 15)*.

[14] Sreeprasad, T. S. and Pradeep, T., (2013). “Noble Metal Nanoparticles”. In Vajtai, R. (Eds), *Springer Handbook of Nanomaterials* (pp. 303 - 388).

[15] N.D. “Surface Plasmon”. Retrieved from https://pdfs.semanticscholar.org/2e15/bebe7031fe29930b676017028d845dcbf042.pdf.

[16] Kumar, Narenda and Kumar, Rajiv. (2014). "Chapter 2 - Nano-based Drug Delivery and Diagnostic Systems". *Journal of Nanotechnology and Nanomaterials in the Treatment of Life-threatening Diseases,* pp 53-107.

[17] Parmar, Chetan K., Rumbles, Garry and Winscomb, Christopher J. (2002). "Aggregation of azamethine dyes on hydrated glass surfaces: An evanescent wave-induced fluorescence study". *Physical Chemistry Chemical Physics,* Vol 10, pp. 1766-1775.

[18] Long, Yi-Tao and Jing, Chao. (2014). "Localized Surface Plasmon Resonance Based Nanobiosensors".

[19] Freestone, I., Meeks, N., Sax, M., and Higgitt, C. (2008). “The Lycurgus Cup - A Roman nanotechnology,” *Gold Bulletin*.

[20] Blackie, E. J., Le Ru, E. C., and Etchegoin, P. G. (2009). “Single-molecule surface-enhanced raman spectroscopy of nonresonant molecules,” *J. Am. Chem. Soc.,* vol. 131, no. 40, pp. 14466–14472.

[21] Krutyakov, Y. A., Kudrinskiy, A. A., Olenin, A. Y., and Lisichkin, G. V. (2008). “Synthesis and properties of silver nanoparticles: advances and prospects,” *Russ. Chem. Rev.*, vol. 77, no. 3, pp. 233–257.

[22] Darvill, D., Centeno, A., and Xie, F. (2013). “Plasmonic fluorescence enhancement by metal nanostructures: shaping the future of bionanotechnology,” *Phys. Chem. Chem. Phys.*, vol. 15, pp. 15709–15726.

[23] Maier, Stefan A. (2007). Plasmonics: Fundamentals and Applications.

[24] Born, Max and Wolf, Emil. (1999). Principles of Optics.

[25] Baffou, Guillaume. (2018). Thermoplasmonics: Heating Metal Nanoparticles Using Light, pp 7 – 9.

[26] Christensen, Thomas. (2017). From Classical to Quantum Plasmonics in Three and Two Dimension, pp 26-27.

[27] Ringe, Emilie, Zhang, Jian, Langille, Mark R., Mirkin, Chad A., Marks, Laurence D., dan Van Duyne, Richard P. Nanoteknologi 23, 444005.

[28] Harrison, R. K. (2012). "Mechanisms and applications of near-field and far-field enhancement using plasmonic nanoparticles," The University of Texas at Austin.

[29] Hirvonen, J.K, (1980). "Ion Implantation". In Hirvonen, J.K. (Eds), *Treatise on Materials Science and Technology* (pp 1 – 16).

[30] Nastasi, M. and Mayer, J. W. (2006). "Ion Implantation and Synthesis of Materials" pp 1 – 10.

[31] William, J.S. and Poate, J. M. 1984. "Introduction to Implantation and Beam Processing". In William and Poate (Eds), *Ion Implantation and Beam Processing* (pp 1 – 11).

[32] Nuclear Physics Department & Tandem Accelerator Department. (2019). 9 MV FN Pelletron Tandem Accelerator. Retrieved from https://tandem.nipne.ro/9MV_Pelletron.php.

[33] Tkachenko, Nikolai V. (2006). "Optical Spectroscopy: Methods and Instrumentations" pp 99 - 102.

[34] Verma, H.R. 2007. "Chapter 2 Rutherford Backscattering Spectroscopy". *Atomic and Nuclear Analytical Methods*. pp 91 – 142.

[35] Oh, Kyuhak and Christenson, Michael P. (2019). "Design of an automated particle detection system for Rutherford backscattering (RBS) using LabVIEW". *Instrumentation Science & Technology*. VOL. 47, NO. 3, pp 312–324.

[36] EA Laboratories. (2019). "RBS Tutorial: Theory". Retrieved from https://www.eag.com/resources/tutorials/rbs-tutorial-theory/.

[37] Mayer, Matej. (2017). SIMNRA User's Guide (This document describes SIMNRA version 7.01).

[38] Royal Society of Chemistry. (2019). "Introduction to Ultraviolet - Visible Spectroscopy (UV)". Retrieved from http://www.rsc.org/learn-chemistry/content/filerepository/CMPARTICLES/00/001/304/UV/Vis_Student%20resource%20pack_ENGLISH.pdf.

[39] Horikoshi, Satoshi. and Serpone, Nick. (2013) "Introduction to Nanoparticles," in *Microwaves in Nanoparticle Synthesis: Fundamentals and Applications*, pp 1-24.

[40] Abdelhalim, M. A. K., Mady, M. M and Ghannam, M. M., (2012). “Physical Properties of Different Gold Nanoparticles: Ultraviolet - Visibleand Fluorescence Measurements”. Journal of Nanomedicine & Nanotechnology.

[41] Rechberger, W., Hohenau, A., Leitner, A., Krenn, J.R., Lamprecht, B. and Aussenegg, F.R. (2003). "Optical properties of two interacting gold nanoparticles". *Optics Communications* 220, pp 137–141.